This article has been accepted for publication in a future issue of this journal, but has not been fully edited. Content may change prior to final publication. Citation information: DOI 10.1109/TPWRD.2020.3016279, IEEE Transactions on Power Delivery

Subcycle Overvoltage Dynamics in Solar PVs

Lingling Fan, *Senior Member, IEEE*, Zhixin Miao, *Senior Member, IEEE*, and Miao Zhang, *Student Member, IEEE*

***Abstract*—In 2017 and 2018, bulk power system (BPS) connected solar photovoltaic (PV) inverters tripped after grid disturbances in South California, causing large-scale power loss. One cause of PV tripping is subcycle overvoltage experienced by PV inverters when the grid suffers voltage dip and PVs enter into momentary cessation. This paper examines the underlying mechanism of the subcycle overvoltage dynamics. A dq-frame analytical model is built for a PV grid-integration system with a focus on the grid side converter (GSC) and grid interaction. PV's dc circuit dynamics and controls are ignored. Eigenvalue analysis indicates that two modes cause the subcycle overvoltage. The modes are associated with shunt compensation, grid electromagnetic dynamics, and PV inverter controls. Furthermore, a more insightful explanation of subcycle overvoltage is offered relying on s-domain admittance models. The dq-frame admittance is derived for the PV viewed from the point of common coupling (PCC). A circuit model relying on the derived admittance can demonstrate subcycle overvoltage due to momentary cessation. Impacts of grid strength, phase-locked-loop (PLL) parameters and converter current control parameters are all examined. It is found that the inherent LC dynamics due to shunt compensation and grid inductance are the main dynamics that can cause overvoltage, and momentary cessation excites overvoltage dynamics.**

***Index Terms*—Solar Photovoltaic (PV) grid integration; voltage source converter (VSC); subcycle overvoltage dynamics; admittance model**

I. Introduction

SOLAR PV penetration in power grids increases over time. PV systems experience various dynamics due to transmission grid disturbances. From 2016 to 2018, bulk power system (BPS) connected solar photovoltaic (PV) inverters tripped after large grid disturbances in South California [1]–[3]. The major cause for PV tripping in the 2017 Cayon 2 fire event is identified as overvoltage experienced by PV inverters within subcycle when the transmission grid experienced voltage dip due to faults. Inverter protection devices are suggested to have filters to filter out transient overvoltage and avoid such tripping.

The subcycle dynamics in PV farms during large transmission grid disturbances, are not well understood according to the NERC reports (page 6 of [2]). Recommendations have been given in [2] to industry to conduct more studies to better understand subcycle transient overvoltage.

The objective of this paper is to investigate the mechanism of subcycle overvoltage dynamics. To the authors' best knowledge, this is the first research paper to address the particular dynamics.

The investigation employs large-signal simulation and the classical linear system analysis. First, we demonstrate the dynamics using two electromagnetic transient (EMT) testbeds with full details. While the EMT testbeds are suitable for demonstration and validation, they are not feasible for small-signal analysis which can offer invaluable insights [4], [5]. Thus, a nonlinear analytical model is built with the capability of both large-signal simulation and small-signal analysis.

In the literature, nonlinear state-space model of PV systems has been constructed in [6], [7]. The PV system model in [6], [7] includes grid-connected voltage source converter (VSC) feedback controls, DC/DC boost converter controls, maximum power point tracking (MPPT) and irradiance-driven dynamics. Whilst the model is comprehensive in modeling the PV side of the system, the model adopts an assumption that the PCC voltage is a stiff voltage source and it employs a single dq-frame for modeling. Hence, this model is not feasible to consider the influence of grid strength on PV system dynamics.

The analytical model built in the authors' previous research for wind in weak grid [8]–[11] is adopted in this research. This model has the PV system dc side dynamics ignored but has the capability to consider the influence of grid strength by using two dq-frames: the grid frame and the PLL frame. Thus, grid strength effect and PLL dynamics' influence can be adequately modeled. Also in the literature, linear state-space models of VSC grid integration systems were mathematically derived in [12], [13] . While those models can be used for eigenvalue and participation factor analysis, those models are not suitable for large-signal analysis. On the other hand, our analytical model can be used for both large-signal simulation and small-signal analysis.

Further, a more insightful explanation of subcycle overvoltage dynamics is sought, relying on the s-domain admittance model based circuit analysis. By viewing PV as a Norton circuit (a current source with a parallel s-domain admittance), a circuit model is built. The effect of momentary cessation can be captured by the circuit model and subcycle overvoltage can be demonstrated in the PCC voltage. Impacts of grid strength, PLL parameters and converter current control parameters are all examined.

s-domain impedance/admittance models for grid-connected inverters have been seen in the literature with PLL's effect included, e.g., [14]–[16]. We adopt the same approach for admittance derivation. Nevertheless, using Norton equivalent to construct a circuit representing PV grid-integration system for subcycle overvoltage dynamic analysis is a unique contribution.

In summary, the contribution of this paper is two-fold.

- Subcycle overvoltage dynamic phenomenon is successfully replicated and analyzed via a state-space nonlinear PV grid integration model. This model not only demonstrates subcycle overvoltage due to momentary cessation,

This project is supported in part by US Department of Energy SETO DE-EE-0008771.

L. Fan, Z. Miao, and M. Zhang are with the Department of Electrical Engineering, University of South Florida, Tampa, FL, 33620. e-mail: linglingfan@usf.edu

This article has been accepted for publication in a future issue of this journal, but has not been fully edited. Content may change prior to final publication. Citation information: DOI 10.1109/TPWRD.2020.3016279, IEEE Transactions on Power Delivery

but also offers invaluable insights on the dynamic phenomenon via eigenvalue analysis and participation factor analysis.
- s-domain admittance-based circuit analysis leads to the discovery of subcycle overvoltage mechanism. Subcycle overvoltage is due to momentary cessation of PV inverters which excites the inherent LC dynamics of the system, where C is related to the PV shunt compensation and L is related to the grid's Thevenin equivalent inductance.

The rest of this paper is organized as follows. Section II introduces two EMT testbeds: a 400-kW PV farm grid integration system (EMT testbed 1) and a 25-MW PV grid integration system (EMT testbed 2). The two testbeds employ different converter control parameters. In addition, EMT testbed 1 employs average model for converters while EMT testbed 2 includes power electronics switching details. The occurrence of subcycle overvoltage further indicates that control parameters have negligible influence on the occurrence of subcycle overvoltage dynamics.

The state-space nonlinear analytical model representing EMT testbed 1 is also described in Section II. Section III presents the subcycle overvoltage demonstration of the EMT testbeds, followed up with eigenvalue analysis and subcycle overvoltage demonstration using the analytical model. Section IV presents the s-domain admittance-based circuit model and the related analysis. Finally, conclusions are given in Section V.

II. PV Testbeds and Analytical Model

Two EMT testbeds are examined: one adopts average converter model while the other has full details of converter switching. While PV inverters in both testbeds are grid-following converters, they have different control parameters. Also the converters' control structures have subtle difference. Testbed 1 has voltage feedforward filter while Testbed 2's feedforward has no filter. The utilization of the two testbeds is to examine how much influence converter control may have on subcycle overvoltage occurrence.

A. EMT Testbed 1 in MATLAB/SimPowerSystems

A PV farm grid integration testbed, which is based on the 400-kW grid-connected PV farm demo in MATLAB/SimPowerSystems, is used for validation. The topology diagram is shown in Fig. 1. There are four PV arrays connected in parallel. Each array has a capability of delivering a maximum of 100 kW at 1000 W/m^2 sun irradiance. A single PV array block consists of 64 parallel strings, with each string having five SunPower SPR-315E modules connected in series.

The four PV arrays are connected to four DC/DC boost converters, respectively. Perturb and observe-based MPPT is implemented in the DC/DC boost converters to regulate the PV array voltage (V_{PV}) at 260 V level. The output voltage level of the DC/DC boost converters is 500 V dc. The dc voltage is converted to a three-phase 260 V ac voltage through a VSC, marked in the figure as grid-connected converter (GSC). Shunt compensation (notated as C_1) is employed at the PCC bus for reactive power compensation. The PV is connected to a 25 kV line through a step-up transformer, and further to a 120 kV grid through another step-up transformer. 25% shunt compensation is assumed. The parameters of Testbed 1 can be found in Table I.

This testbed has full EMT and control dynamics modeled, including DC/DC converter control for MPPT, VSC control, and grid dynamics. For converters, average models are adopted. In Sections III and IV, the simplified analytical model and derived admittance model are proposed based on this testbed's parameters.

TABLE I: 400 kW PV farm testbed parameters

Description	Parameters	Value
Power base	S_b	400 kW
Voltage base	ac side	260 V, 25 kV
Voltage base	dc side	500 V
Power level	P_{PCC}	0.937 pu
Converter filter	R_1	$0.15/50$ pu
	X_1	0.15 pu
Shunt Capacitor	$C_1(B_1)$	0.25 pu
DC-link Capacitor	C_{dc}	0.05 F
PV LC filter	L_{pv}, C_{pv}	5 mH, 100 μF
Transmission line	R_g	$0.1X_g$
Current control loop	K_{pi}, K_{ii}	$(0.3, 5)$ pu
DC-link control loop	K_{pp},K_{ip}	$(1, 100)$ pu
AC voltage control	K_{pv}, K_{iv}	$(1, 100)$ pu
PLL	$K_{p,\mathrm{PLL}}$, $K_{i,\mathrm{PLL}}$	$(60, 1400)$ pu
VFF filter	T_{VF}	0.001 s

B. EMT Testbed 2 in PSCAD

TABLE II: 25 MW PV farm PSCAD testbed parameters

Description	Parameters	Value
Switching frequency	3 kHz (VSC)	5 kHz (DC-DC)
Power base	S_b	25 MW
Inverter power base	S'_b	250 kW
Inverter dc voltage base	$V_{\mathrm{DC,b}}$	1 kV
PCC voltage base	$V_{\mathrm{PCC,b}}$	0.55 kV
POC voltage base	$V_{\mathrm{POC,b}}$	33 kV
Power level	P_{POC}	1 pu
System frequency	f_b	60 Hz
LCL filter	L_{filter}, C_{filter}	0.32 mH, 54.80 μF
Damper	L_{damp}, C_{damp}, R_{damp}	1.60 mH, 27.40 μF, 7.65 Ω
Shunt capacitor	B_{C1}	0.2 pu
DC-link capacitor	C_{dc}	10000 μF
PV LC filter	L_{pv}, C_{pv}	2.5 mH, 100 μF
Transformer impedance	X_{T1}	0.05 pu
Transmission line	X_g, R_g	0.45 pu, 0.05 pu
Current control loop	K_{pi}, K_{ii}	$(0.2, 20)$ pu
DC-link control loop	K_{pp}, K_{ip}	$(1, 20)$ pu
V_{ac} control loop	K_{pv}, K_{iv}	$(1, 10)$ pu
PLL	$K_{p,\mathrm{PLL}}$, $K_{i,\mathrm{PLL}}$	$(500, 200)$ pu

Another 25-MW PV system testbed is adopted to observe the subcycle overvoltage dynamics. This model was developed and posted by PSCAD [17]. The system topology is shown in Fig. 3. The solar farm consists of 100 PV arrays. Each unit generates a maximum power of 0.25 MW at the nominal irradiation of 1000W/m^2 and nominal temperature of 28 degrees celcius. The MPPT, detailed DC/DC boost converter, and detailed three-phase switches are included, shown as Fig. 4. The system parameters are given in Table II.

The base voltage on dc side is 1 kV. The dc voltage is converted to 0.55 kV ac voltage through GSC. Fig. 4 shows the detailed IGBT switches are adopted in the GSC. In the GSC outer control, V_{dc} and V_{PCC} are regulated on d-axis and q-axis,

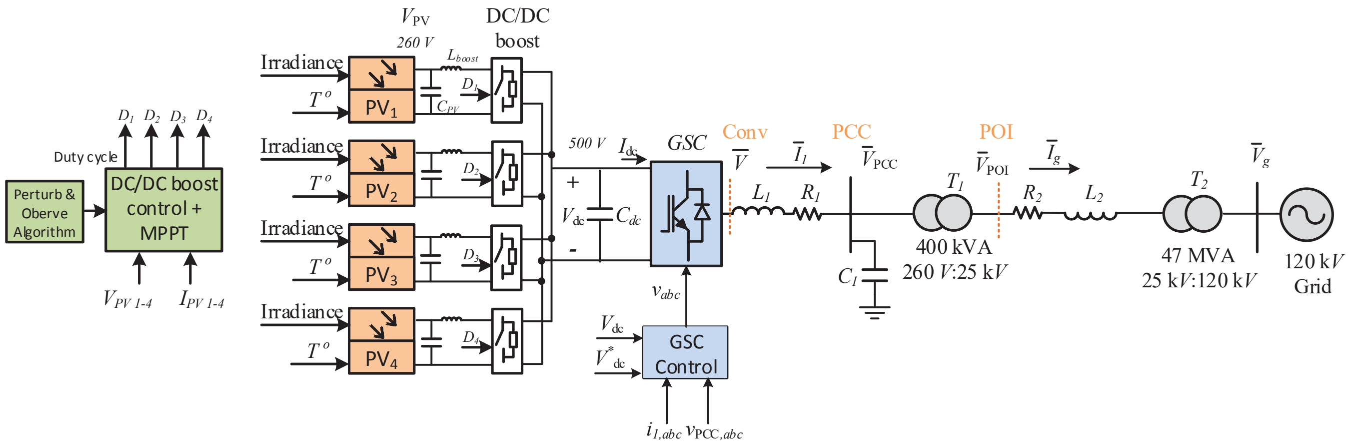

Fig. 1: EMT testbed 1: 400-kW PV farm in Matlab/SimPowersystms.

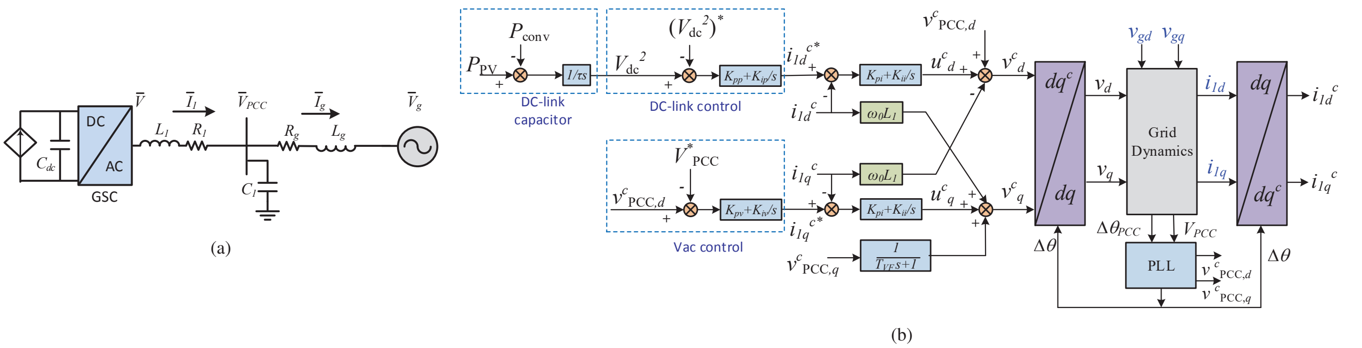

Fig. 2: (2a) Simplification by treating left of the dc-link as a controlled current source to provide constant power. (2b) Block diagram of the dq-frame based analytical model.

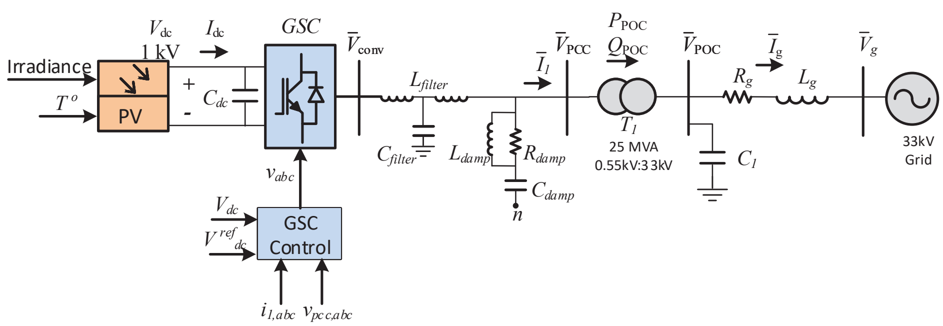

Fig. 3: EMT testbed 2: 25-MW PV solar farm in PSCAD.

respectively. There is no voltage feedforward filter added in the GSC inner current control. A damper along with a LCL filter are used to minimize the impact of harmonics generated by the switches. Note that the $C_{\rm damp}$ has very small compensation effect on system, i.e., 0.85% pu. A transformer with 0.05 pu inductive reactance is to boost the voltage level from 0.55 kV (PCC) to 33 kV (POC). A 20% shunt capacitor is connected on POC bus.

C. Analytical Model

The analytical model considers VSC grid integration. VSC dc-link capacitor C_{dc} is explicitly modeled with input power P_{PV} treated as a known parameter. Dc/dc boost converter, MPPT and PV electrochemical characteristics have been ignored. The simplified system is shown in Fig. 2a. R_g and L_g represent the aggregated resistance and inductance of transformers and distribution line.

Analytical models of the VSC grid integration system have been built in the authors' prior work [8] and employed for analysis of wind in weak grids [9]–[11]. This model is based on two dq-reference frames. All state variables assume constant values at steady-state. Thus, it is possible to use numerical perturbation to extract linear models.

The block diagram of analytical model is shown in Fig. 2b. The model is based on two dq-frames: the grid frame and the converter frame, notated by superscript c. The grid voltage is assumed to have a constant nominal frequency and a phase

This article has been accepted for publication in a future issue of this journal, but has not been fully edited. Content may change prior to final publication. Citation information: DOI 10.1109/TPWRD.2020.3016279, IEEE Transactions on Power Delivery

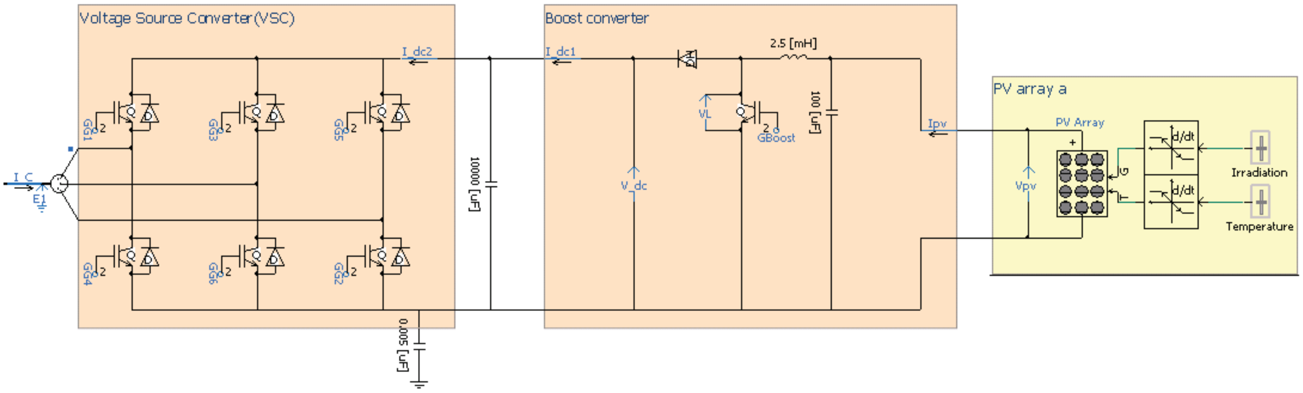

Fig. 4: EMT testbed 2: Inverter and DC/DC booster topology with switches.

angle 0. Therefore, the angle between its space vector and the static frame is $\omega_0 t$, where ω_0 is the nominal frequency (377 rad/s). d-axis of the grid-frame is aligned with the grid voltage space vector. The converter frame is aligned with the sensed PCC voltage space vector. The angle of the PCC voltage space vector (notated as $\theta_{\rm PCC}$) is sensed by PLL as shown in Fig. 5(a). Output of the PLL is θ and this angle tracks the PCC voltage angle $\theta_{\rm PCC}$. The d-axis of the converter frame is ahead of the static frame by an angle. This angle is the PLL output angle θ. Fig. 5(a) is the three-phase PLL adopted in the EMT testbeds.

Fig. 5 (b) presents the linearized model of the PLL with the assumption that the PCC voltage magnitude is at 1 pu and the PLL tracks the PCC voltage angle closely. $\Delta\theta_{\rm PCC} = \theta_{\rm PCC} - \omega_0 t$ and $\Delta\theta = \theta - \omega_0 t$.

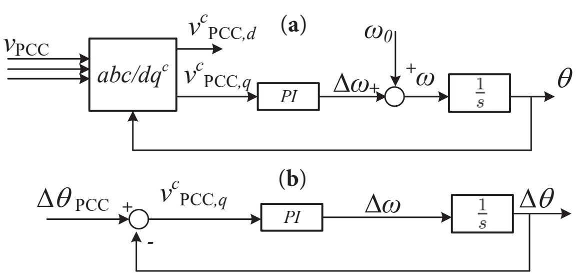

Fig. 5: Synchronous frame based PLL: nonlinear model and linear model.

Since the converter frame is based on the PLL output angle, it is also named as the PLL frame. The angle between the PLL frame and the grid frame is notated as $\Delta\theta$, where $\Delta\theta = \theta - \omega_0 t$. Fig. 6 presents four frames: the static frame, the grid frame used in the analytical model (notated as Grid frame 1), the PLL frame, and another grid frame notated as Grid frame 2. Grid frame 2 will be used in Section IV.

The converter's vector control is based on the PLL frame or the converter frame, which consists of outer control to regulate dc-link voltage and ac voltage at PCC, and inner current control. The dc-link voltage control generates d-axis current order while the ac voltage control generates q-axis current order. The inner current control tracks the current orders and generates VSC voltage order v_d^c and v_q^c. The voltage

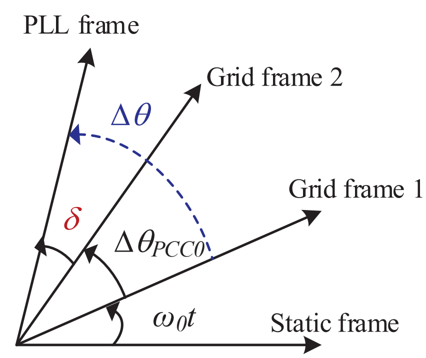

Fig. 6: Four frames: static, grid frame 1, grid frame 2, and PLL frame.

feedforward (VFF) units are employed in both axes. In Fig. 2b, the q-axis VFF includes a low-pass filter with time constant $T_{\rm VF}$.

While the converter control is based on the converter frame, the grid dynamics are modeled in the grid frame. The d-axis of the grid frame is aligned with the grid voltage. The system parameters are given in Table I.

III. Subcycle Dynamics: Demonstration and Eigenvalue Analysis

The NERC report [2] indicates that when PV inverters sense voltage drop, PV inverters immediately reduce its current injection to 0. This stage is termed as "momentary cessation": PV inverters are connected to the grid while injecting zero currents to the grid.

A. Demonstration in the EMT testbeds

1) MATALB/SimPowerSystems testbed: Simulation is carried out using the EMT testbed 1. At $t = 1$ second, the grid voltage experiences 0.1 pu drop. Immediately, the current orders of the VSC reduce to 0. After 0.04 seconds, the grid voltage recovers. The converter voltage, PCC voltage, point of interconnection (POI) voltage and the grid voltage are plotted together. The POI voltage is assumed to be measured at the 25 kV side of the transformer and the transformer is assumed

This article has been accepted for publication in a future issue of this journal, but has not been fully edited. Content may change prior to final publication. Citation information: DOI 10.1109/TPWRD.2020.3016279, IEEE Transactions on Power Delivery

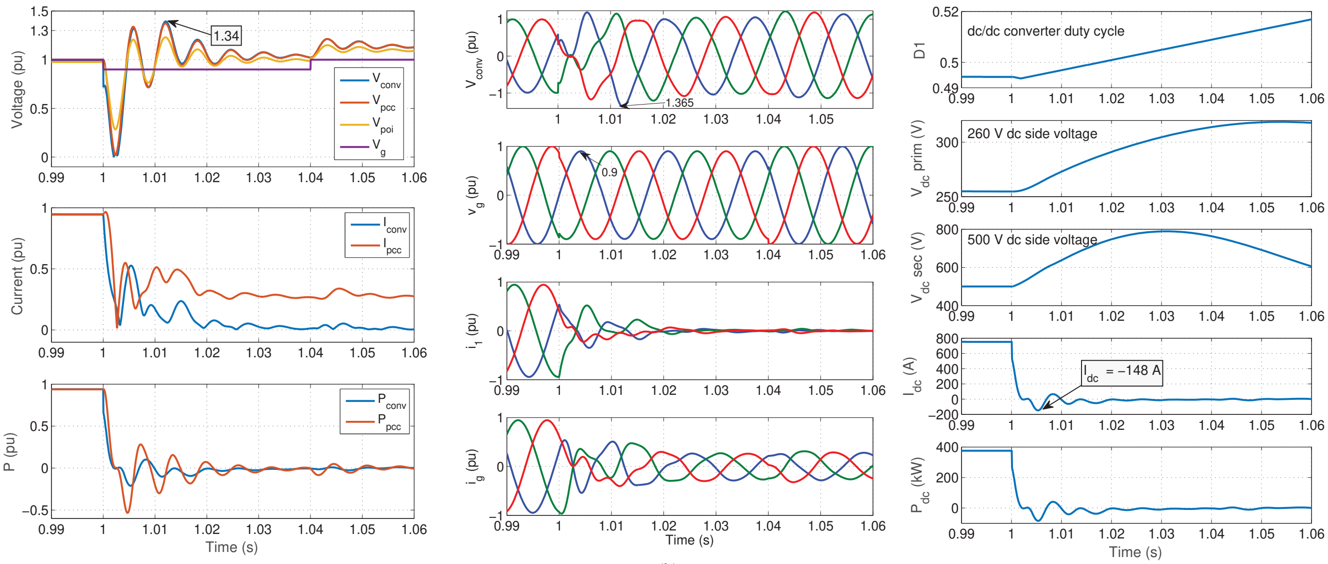

(a) (b) (c)

Fig. 7: Simulation results from the EMT testbed 1 in Matlab/SimPowersystems. PV enters momentary cessation after 1 second. (7a) GSC ac side voltage magnitudes, current magnitudes and real power. (7b) GSC ac side three-phase converter voltage, grid voltage, converter current, and grid current. (7c) DC/DC converter duty cycle, 260 V dc-side voltage, 500 V dc side voltage, dc current, and dc power to the grid from the converter.

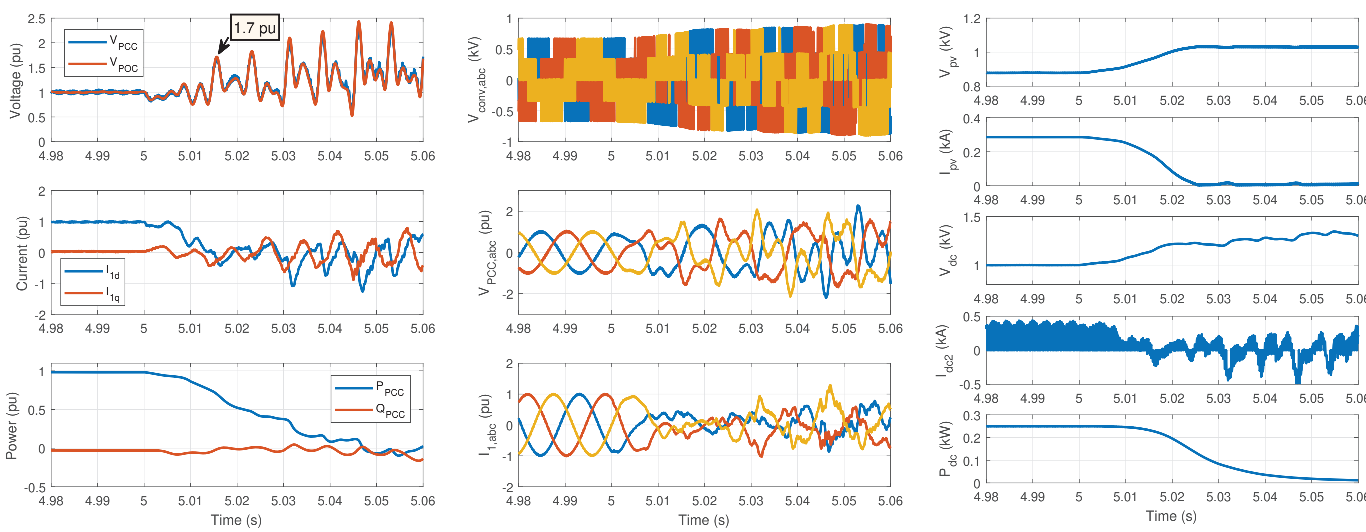

(a) (b) (c)

Fig. 8: Simulation results from the EMT testbed 2 in PSCAD. PV enters momentary cessation after 5 seconds. (a) GSC ac side PCC voltage, POC voltage, converter current, and PCC power. (b) Three-phase converter voltage, PCC voltage, and converter current. (c) PV voltage and current magnitude, dc-link voltage and current magnitude, and the output power from the DC-DC booster.

to have a reactance at 0.15 pu. The total reactance from the PCC bus to the grid X_g is selected to be 0.5 pu.

Fig. 7 presents the simulation results of ac side voltage magnitudes, current magnitudes, power, three-phase voltage and current waveforms, and dc-side control variables and measurements (DC/DC converter duty cycle ratio D_1, 260 V dc side voltage, 500 V dc side voltage, dc current and power measured between the dc-link capacitor and the VSC). It can be observed that 0.1 pu voltage dip in the grid voltage results in 1.34 pu overvoltage in the converter voltage. In addition, reverse dc current has been observed during the subcycle dynamics.

2) PSCAD testbed: At $t = 5$ seconds, the momentary cessation is applied in PSCAD PV testbed. The simulation results are shown in Fig. 8. The PCC bus and POC bus voltage magnitudes, converter current in dq-frame, and power on POC bus are plotted in Fig. 8(a). The three-phase converter voltage, PCC bus voltage and converter current are plotted in Fig. 8(b). The dc side voltage and current are plotted in Fig. 8(c).

Fig. 8(a) shows that 1.71 pu overvoltage can be observed on the PCC bus. The three-phase converter voltage plot indicates the detailed inverter switches result in significant harmonics.

This article has been accepted for publication in a future issue of this journal, but has not been fully edited. Content may change prior to final publication. Citation information: DOI 10.1109/TPWRD.2020.3016279, IEEE Transactions on Power Delivery

The filter and damper can filter out the high-frequency harmonics.

Remarks: Both EMT testbeds, based on average model or full switching details, can demonstrate the occurrence of subcycle overvoltage due to momentary cessation. The two testbeds have very different converter control parameters, which indicates that converter control parameters play an insignificant role in the occurrence of subcycle dynamics.

B. Eigenvalue analysis and demonstration based on the analytical model

EMT Testbed 1: Relying on the analytical model, linear models can be extracted using numerical perturbation at certain operating condition. For EMT Testbed 1 at the operation condition of 1 pu PCC voltage, 1 pu grid voltage, and 0.937 real power dispatch, linear models are extracted for different X_g to examine the effect of grid strength on dynamics. In addition, the analytical model is assumed to operate at the beginning of momentary cessation stage, i.e., the outer control loops are no longer functioning. Instead, the converter control is under current control only.

Fig. 9 present eigenvalue loci for a varying X_g. It can be found that there are two modes in the range of $60 \sim 200$ Hz. These modes are sensitive to the current control parameters, grid reactance X_g, and the shunt compensation level. With X_g increasing, the two modes move to the right half plane, which indicates that weaker grid strength may cause more severe dynamics. The participation factor table of the two modes is presented in Table III. It can be seen that the 200 Hz mode (mode 1) is heavily influenced by the PCC voltage and converter current. The 60 Hz mode (mode 2) is influenced by the line and converter currents as well as the feedforward filter.

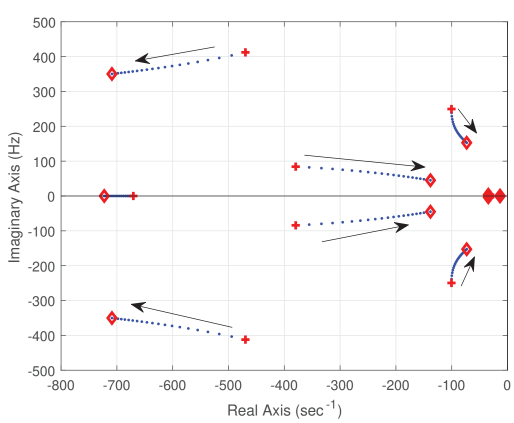

Fig. 9: Eigenvalues. X_g varies from 0.26 to 0.60 pu, with each step 0.02 pu.

The same event is applied on the analytical model to carry out time-domain simulation. Fig. 10 presents voltages at different locations. It can be seen that the oscillation frequency is about 200 Hz. When the grid is weaker, overvoltage is more severe. For this system, when X_g is at 0.50 pu, the voltage at inverter can reach 1.4 pu.

EMT Testbed 2: Analytical model-based simulation and eigenvalue analysis are also carried out using EMT Testbed 2's parameters. Fig. 11 presents the time-domain simulation results for momentary cessation. Subcycle overvoltage is observed. Eigenvalue analysis results are presented in Fig. 12(a). It can be seen that the system has two modes: one at 133 Hz and the other at 266 Hz.

TABLE III: Participation factors (PF) of modes

Description	State variable	mode 1	mode 2
Grid Dynamic	i^g_{1d}	0.0272	0.1461
	i^g_{1q}	**0.4276**	**0.2229**
	i^g_{gd}	0.0225	0.0597
	i^g_{gq}	0.1162	**0.6571**
	$v^g_{pcc,d}$	0.0423	0.1176
	$v^g_{pcc,q}$	**0.4898**	0.0991
PLL	$\Delta\omega$	0.0122	0.1195
	$\Delta\theta$	0.0001	0.0077
Feedforward filter	$v^c_{pcc,q}$	**0.1748**	**0.4846**
Current controller	u^c_d	0.0001	0.0135
	u^c_q	0.0010	0.0182

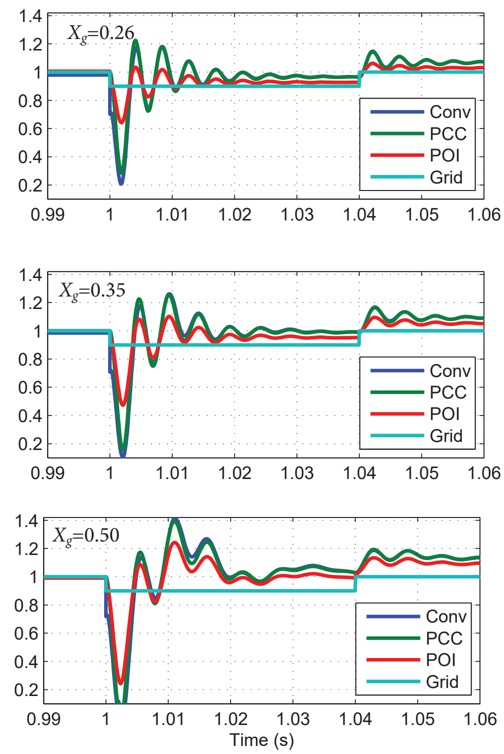

Fig. 10: Simulation results of voltages at different locations via the analytical model. PV enters momentary cessation after 1 second.

The high-order harmonics in V_{PCC}, abc voltages in Fig. 8(a) are indeed caused by the 133 Hz mode and the 266 Hz mode. The FFT analysis results of V_{PCC} are shown in Fig. 12 (b). The FFT analysis is conducted from 5.0 s to 5.06 s for the PSCAD simulation data. The FFT analysis is conducted on the analytical model based simulation data from 1.0 s to 1.06 s. The FFT analysis confirms that 133 Hz and 266 Hz modes are major components for subcycle dynamics. Participation factor analysis (results are not presented in the paper) confirms that the 266 Hz mode is related to LC dynamics while the 133 Hz mode is related to the converter current as well as converter control.

Remarks: The analysis and simulation results show that the

This article has been accepted for publication in a future issue of this journal, but has not been fully edited. Content may change prior to final publication. Citation information: DOI 10.1109/TPWRD.2020.3016279, IEEE Transactions on Power Delivery

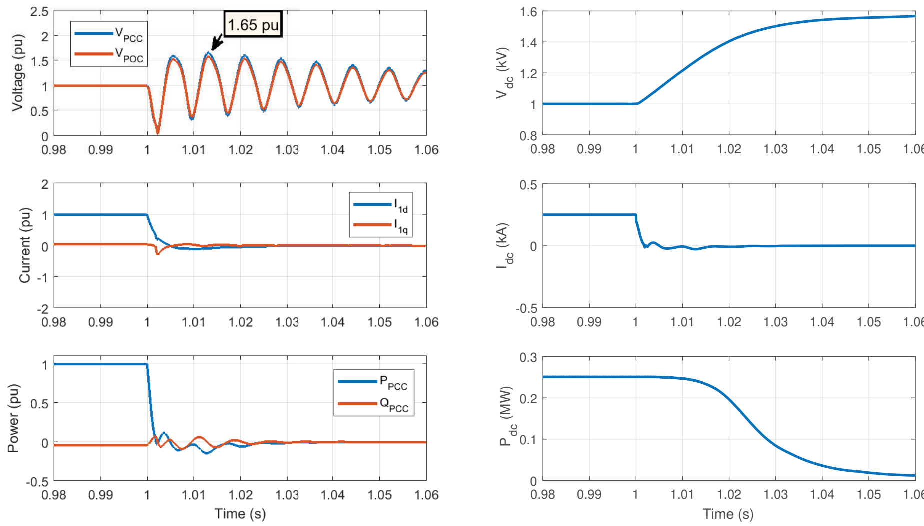

(a)

(b)

Fig. 11: Dynamic simulation results of the analytical model using EMT Testbed 2 parameters. (a) AC side PCC voltage, POC voltage, converter current, and PCC power. (b) DC side voltage, current, and the input dc power.

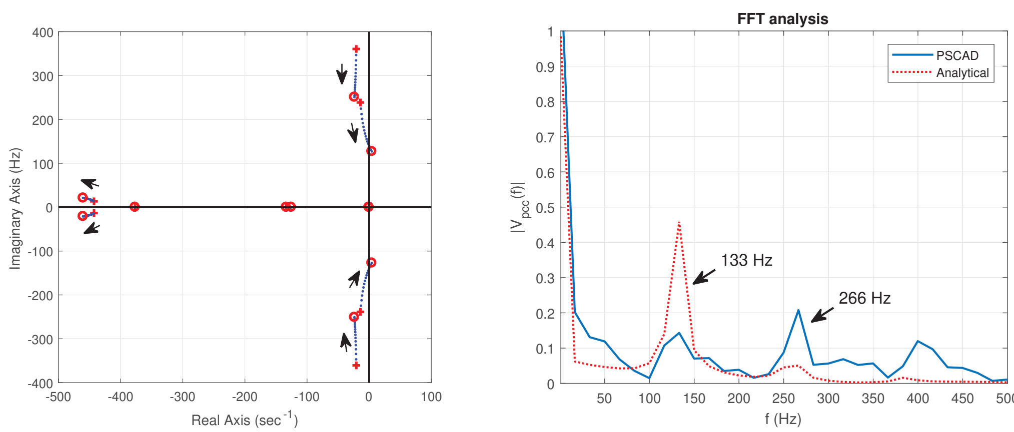

(a)

(b)

Fig. 12: Eigenvalue analysis results and FFT analysis results. (a) Eigenvalue: X_g varies from 0.2 to 0.5 pu, with each step 0.02 pu. (b) FFT analysis on PSCAD and analytical PCC bus voltage.

subcycle overvoltage dynamics are related to grid dynamics which is influence by the PV farm shunt compensation and grid inductance. The inter-relationship between shunt compensation, subcycle overvoltage and momentary cessation has been identified as Finding 8 in [2]. The eigenvalue analysis confirms the finding.

IV. Circuit Model Based on Admittances

In this section, a more insightful explanation of subcycle overvoltage dynamics is sought using circuit model. The PV farm is now viewed as a Norton circuit with the converter current order reflected as a current source and converter controls and RL filter as an admittance. Fig. 13 presents the circuit model that is desired. Using the circuit model, momentary cessation can be represented as step changes in the current source. Thus, PCC voltage dynamic response can be found using circuit analysis. Derivation of VSC admittance has been carried out in the literature since 2007 in [14]. For this research, accurate representation of converter under momentary cessation is desired. During momentary cessation, the converter works under current control only. Thus, PLL and current control details should be modeled. Furthermore, to achieve concise expressions, selection of grid-frame is very important. In this research, the approach used in [18] is adopted for grid-frame selection. Grid frame 2 shown in Fig. 6 is used as the grid frame.

A. Admittance Model of the PV Viewed at the PCC Bus

Based on the current control loop relationship show in Fig. 2b, the following relationship of the converter voltage, PCC voltage, and converter current in the PLL frame can be found.

This article has been accepted for publication in a future issue of this journal, but has not been fully edited. Content may change prior to final publication. Citation information: DOI 10.1109/TPWRD.2020.3016279, IEEE Transactions on Power Delivery

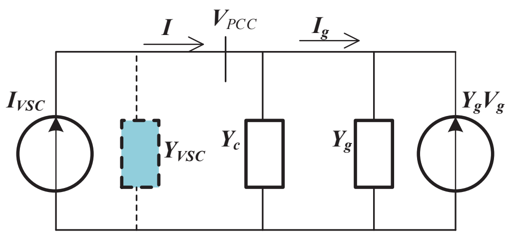

Fig. 13: Circuit model of a PV grid integration system. PV is represented by a Norton equivalent: a current source with a parallel admittance $\mathbf{Y}_{\mathrm{VSC}}$. If the PLL effect and feedforward filter are ignored, the PV will be a current source only.

$$\begin{aligned}\begin{bmatrix}\Delta v_d^c\\ \Delta v_q^c\end{bmatrix} = &-\underbrace{\begin{bmatrix}K_{pi}+\frac{K_{ii}}{s} & \omega_0 L_1\\ -\omega_0 L_1 & K_{pi}+\frac{K_{ii}}{s}\end{bmatrix}}_{Z_C}\begin{bmatrix}\Delta i_{1d}^c\\ \Delta i_{1q}^c\end{bmatrix}\\ &+\underbrace{\begin{bmatrix}K_{pi}+\frac{K_{ii}}{s} & 0\\ 0 & K_{pi}+\frac{K_{ii}}{s}\end{bmatrix}}_{K_c}\begin{bmatrix}\Delta {i_{1d}^c}^*\\ \Delta {i_{1q}^c}^*\end{bmatrix}\\ &+\underbrace{\begin{bmatrix}1 & 0\\ 0 & \frac{1}{T_{\mathrm{VF}}s+1}\end{bmatrix}}_{F_F}\begin{bmatrix}\Delta v_{\mathrm{PCC},d}^c\\ \Delta v_{\mathrm{PCC},q}^c\end{bmatrix}\end{aligned} \tag{1}$$

In (1), all voltage and current variables are in the PLL frame. They will be converted to variables in a grid frame. This grid frame rotates at the nominal frequency ω_0. The grid frame variables will be notated without superscript. The d-axis of the grid frame is aligned to the PCC voltage space vector at the steady-state. If the grid voltage has a phase angle at 0, then this grid frame's d-axis is ahead of the static frame by $\omega_0 t + \Delta\theta_{\mathrm{PCC0}}$, where $\Delta\theta_{\mathrm{PCC0}}$ is the initial phase angle of the PCC voltage phasor.

At steady-state, the PLL frame aligns with the grid frame: $\delta = 0$. On the other hand, during dynamics, the two frames have an angle as δ, where δ is related to PLL's output angle θ: $\delta = \theta - \omega_0 t - \Delta\theta_{\mathrm{PCC0}}$.

The **PCC voltage** expressed in the PLL frame is associated with that in the grid frame as follows.

$$\overline{V}_{\mathrm{PCC}}^c = \overline{V}_{\mathrm{PCC}} e^{-j\delta} \approx \overline{V}_{\mathrm{PCC}}(1-j\delta) \tag{2}$$

(2) can be linearized as follows.

$$\Delta\overline{V}_{\mathrm{PCC}}^c = \Delta\overline{V}_{\mathrm{PCC}} - j\Delta\delta\cdot\overline{V}_{\mathrm{PCC}} \tag{3}$$

At steady-state, $\overline{V}_{\mathrm{PCC}}$ is aligned with the grid frame's d-axis. Hence $\overline{V}_{\mathrm{PCC}} = \hat{v}_{\mathrm{PCC}}$. In the real domain, the PCC voltage deviation can be expressed as follows.

$$\begin{bmatrix}\Delta v_{\mathrm{PCC},d}^c\\ \Delta v_{\mathrm{PCC},q}^c\end{bmatrix} = \begin{bmatrix}\Delta v_{\mathrm{PCC},d}\\ \Delta v_{\mathrm{PCC},q}\end{bmatrix} - \begin{bmatrix}0\\ \hat{v}_{\mathrm{PCC}}\Delta\delta\end{bmatrix} \tag{4}$$

The PLL's control block indicates that

$$\Delta\delta = \underbrace{(K_{p,\mathrm{PLL}} + K_{i,\mathrm{PLL}}/s)(1/s)}_{H(s)}\Delta v_{\mathrm{PCC},q}^c. \tag{5}$$

Combining (4) and (5) leads to the expressions of the q-axis PCC voltage in the PLL frame and the PLL output angle in terms of the q-axis PCC voltage in the grid frame $\Delta v_{\mathrm{PCC},q}$.

$$\Delta v_{\mathrm{PCC},q}^c = \frac{1}{1+\hat{v}_{\mathrm{PCC}}H(s)}\Delta v_{\mathrm{PCC},q} \tag{6}$$

$$\Delta\delta = \frac{H(s)}{1+\hat{v}_{\mathrm{PCC}}H(s)}\Delta v_{\mathrm{PCC},q} \tag{7}$$

$$\begin{bmatrix}\Delta v_{\mathrm{PCC},d}^c\\ \Delta v_{\mathrm{PCC},q}^c\end{bmatrix} = \underbrace{\begin{bmatrix}1 & 0\\ 0 & \frac{1}{1+\hat{v}_{\mathrm{PCC}}H(s)}\end{bmatrix}}_{M_1}\begin{bmatrix}\Delta v_{\mathrm{PCC},d}\\ \Delta v_{\mathrm{PCC},q}\end{bmatrix} \tag{8}$$

The **current phasor** viewed in the PLL frame and that viewed in the grid frame have the following relationship:

$$i_{1d}^c + j i_{1q}^c = (i_{1d} + j i_{1q})\cdot e^{-j\delta} \tag{9}$$

Linearizing (9) leads to the following small-signal model.

$$\Delta i_{1d}^c + j\Delta i_{1q}^c = (\Delta i_{1d} + j\Delta i_{1q}) + (i_{1d} + j i_{1q})\cdot(-j\Delta\delta) \tag{10}$$

Substituting $\Delta\delta$ by (7) leads to the following:

$$\begin{bmatrix}\Delta i_{1d}^c\\ \Delta i_{1q}^c\end{bmatrix} = \begin{bmatrix}\Delta i_{1d}\\ \Delta i_{1q}\end{bmatrix} + \underbrace{\begin{bmatrix}i_{1q}\\ -i_{1d}\end{bmatrix}\cdot\begin{bmatrix}0 & \frac{H(s)}{1+\hat{v}_{\mathrm{PCC}}H(s)}\end{bmatrix}}_{M_2}\cdot\begin{bmatrix}\Delta v_{\mathrm{PCC},d}\\ \Delta v_{\mathrm{PCC},q}\end{bmatrix} \tag{11}$$

Note that the assumption of δ at steady-state is 0 leads to the above concise expression. Should δ is not 0 at steady-state, a coefficient matrix will be multiplied with the grid-frame current in (11).

Similarly, the **converter voltage** in the PLL frame can be expressed as the converter voltage in the grid frame and the PCC voltage in the grid frame.

$$\begin{bmatrix}\Delta v_d^c\\ \Delta v_q^c\end{bmatrix} = \begin{bmatrix}\Delta v_d\\ \Delta v_q\end{bmatrix} + \underbrace{\begin{bmatrix}v_q\\ -v_d\end{bmatrix}\cdot\begin{bmatrix}0 & \frac{H(s)}{1+\hat{v}_{\mathrm{PCC}}H(s)}\end{bmatrix}}_{M_3}\cdot\begin{bmatrix}\Delta v_{\mathrm{PCC},d}\\ \Delta v_{\mathrm{PCC},q}\end{bmatrix} \tag{12}$$

For (1), replace the variables (converter voltage, PCC voltage and converter current) in the PLL frame by those in the grid frame using (8), (12), and (11).

$$\begin{aligned}\begin{bmatrix}\Delta v_d\\ \Delta v_q\end{bmatrix} + M_3\begin{bmatrix}\Delta v_{\mathrm{PCC},d}\\ \Delta v_{\mathrm{PCC},q}\end{bmatrix} &= -Z_c\left(\begin{bmatrix}\Delta i_{1d}\\ \Delta i_{1q}\end{bmatrix} + M_2\begin{bmatrix}\Delta v_{\mathrm{PCC},d}\\ \Delta v_{\mathrm{PCC},q}\end{bmatrix}\right)\\ &+ K_c\begin{bmatrix}\Delta {i_d^c}^*\\ \Delta {i_q^c}^*\end{bmatrix} + F_F\cdot M_1\begin{bmatrix}\Delta v_{\mathrm{PCC},d}\\ \Delta v_{\mathrm{PCC},q}\end{bmatrix}\end{aligned} \tag{13}$$

Note that the PCC voltage and the converter voltage are connected through an RL filter. Hence,

$$\begin{bmatrix}\Delta v_d\\ \Delta v_q\end{bmatrix} = \begin{bmatrix}\Delta v_{\mathrm{PCC},d}\\ \Delta v_{\mathrm{PCC},q}\end{bmatrix} + \underbrace{\begin{bmatrix}R_1+L_1 s & -\omega_0 L_1\\ \omega_0 L_1 & R_1+L_1 s\end{bmatrix}}_{Z_{RL}}\begin{bmatrix}\Delta i_{1d}\\ \Delta i_{1q}\end{bmatrix} \tag{14}$$

Finally, we can have the VSC admittance in (15).

This article has been accepted for publication in a future issue of this journal, but has not been fully edited. Content may change prior to final publication. Citation information: DOI 10.1109/TPWRD.2020.3016279, IEEE Transactions on Power Delivery

$$\underbrace{\begin{bmatrix}\Delta i_{1d}\\ \Delta i_{1q}\end{bmatrix}}_{\mathbf{I}} = \underbrace{(Z_c+Z_{RL})^{-1}K_c\begin{bmatrix}\Delta i_{1d}^{c\ *}\\ \Delta i_{1q}^{c\ *}\end{bmatrix}}_{\mathbf{I_{VSC}}} + \underbrace{(Z_c+Z_{RL})^{-1}(F_F M_1 - I - M_3 - Z_c M_2)}_{-\mathbf{Y_{VSC}}}\underbrace{\begin{bmatrix}\Delta v_{\mathrm{PCC},d}\\ \Delta v_{\mathrm{PCC},q}\end{bmatrix}}_{\mathbf{V}_{\mathrm{PCC}}} \tag{15}$$

It has to be noted that the admittance matrix has a zero column. The dd and qd components are all 0. Fig. 14 presents the Bode plots of the admittance components. It can be seen that the dd, dq components are zero and qq component is dominant. In addition, at the frequency close to 100 Hz to 200 Hz, the qq component has a phase angle at 0 degree, which indicates that the qq component is resistive.

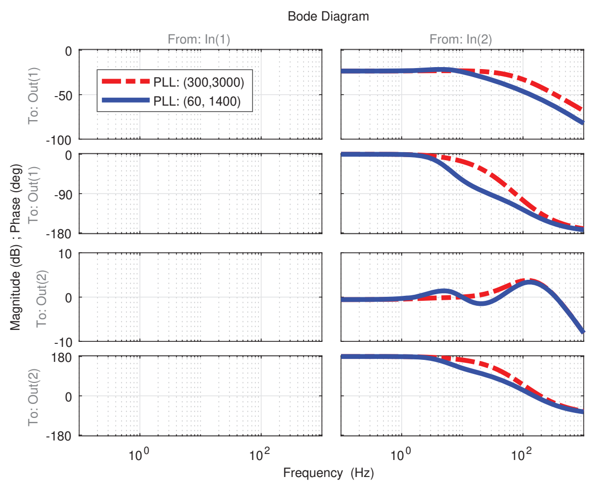

Fig. 14: PV viewed from the PCC bus as an admittance. Only current control and PLL are included. Two sets of PLL parameters are examined.

If the PLL dynamics are ignored and the two frames (the PLL frame and the grid frame) are exactly same, then M_1 is an identity matrix, M_2 and M_3 are $\mathbf{0}$ matrices. If the feedforward filter is ignored, F_F will be an identify matrix. Eq. (15) will be reduced into the following model:

$$\mathbf{I} = \mathbf{I}_{\mathrm{VSC}}. \tag{16}$$

That is, the PV viewed from the PCC bus is a current source only (see Fig. 13). Thus, it can be found that the admittance is due to the effects of PLL and feedforward filter.

B. Validation

The derived admittance matrix of the PV system viewed from the PCC bus assumes only current control. This derived admittance matrix will be compared with the admittance obtained by numerical perturbation of the analytical model shown in Fig. 2b. The measurement testbed is set to have the PCC voltage connected to a grid voltage through a small impedance. The outer controls are all ignored. With the grid voltage as input, the grid current as the output, the input/ouput transfer function matrix is indeed an admittance matrix viewed at the grid.

$$Y = \left((Y_{\mathrm{VSC}}+Y_c)^{-1} + \begin{bmatrix}R_g+L_g s & -\omega_0 L_g\\ \omega_0 L_g & R_g+L_g s\end{bmatrix}\right)^{-1} \tag{17}$$

Fig. 15 presents the Bode plots of the two admittance models. One is obtained based on (15) and (17) and the other is obtained based on numerical perturbation of the analytical model. They show excellent match.

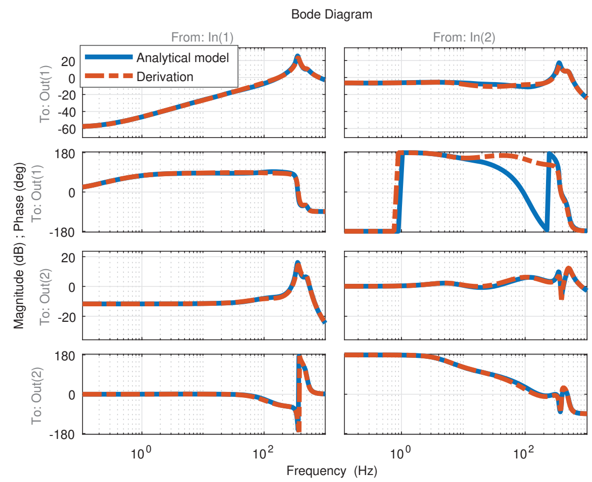

Fig. 15: Comparison of admittance obtained by derivation and numerical perturbation of the analytical model.

C. Circuit Model

The total admittance viewed at the PCC bus is as follows.

$$\mathbf{Y} = \mathbf{Y_{VSC}} + \mathbf{Y_c} + \mathbf{Y_g} \tag{18}$$

where $\mathbf{Y_c} = \begin{bmatrix}C_1 s & -C_1\omega_0\\ C_1\omega_0 & C_1 s\end{bmatrix}$,

and $\mathbf{Y_g} = \begin{bmatrix}R_g+L_g s & -\omega_0 L_g\\ \omega_0 L_g & R_g+L_g s\end{bmatrix}^{-1}$.

Thus, the PCC voltage can be related to the two current sources using circuit analysis:

$$\mathbf{Y}\mathbf{V}_{\mathrm{PCC}} = \mathbf{I}_{\mathrm{VSC}} + \mathbf{Y_g}\mathbf{V_g} \tag{19}$$

where $\mathbf{V}_{\mathrm{PCC}} = \begin{bmatrix}\Delta v_{\mathrm{PCC},d}\\ \Delta v_{\mathrm{PCC},q}\end{bmatrix}$, $\mathbf{V_g} = \begin{bmatrix}\Delta v_{gd}\\ \Delta v_{gq}\end{bmatrix}$, and $\mathbf{I}_{\mathrm{VSC}}$ is defined in (15).

With total current injection to the PCC bus as the input and the PCC bus voltage as the output, the transfer function is $\mathbf{Y^{-1}}$. Thus, the system's eigenvalue is the poles of the transfer function matrix $\mathbf{Y^{-1}}$, or the zeros of the total admittance matrix $\mathbf{Y}$. Matlab function `tzero` can be used to find zeros of s-domain $\mathbf{Y}$ matrix.

In addition, momentary cessation effect on the PCC voltage can be simulated using the linear model. Fig. 16 presents the circuit model-based time-domain simulation results. Before $t = 1$ second, the system is operating at steady-state condition. The PCC voltage dq-axis components are 1 and 0 respectively. The dq-axis components of the converter output current are

0.937 and 0.1176 respectively. At $t = 1$ second, the two converter current orders become 0. In turn, the dq-axis current components experience dynamics and the current magnitude reduces to 0 in less than 0.06 seconds. On the other hand, the PCC voltage experiences overvoltage as shown in Fig. 16. 1.534 pu is reached in less than 0.02 seconds.

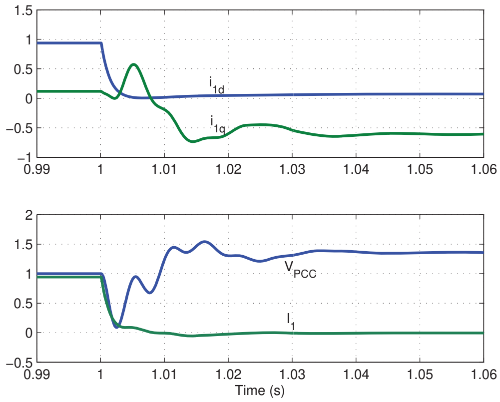

Fig. 16: Momentary cessation effect on the PCC voltage. $X_g = 0.5$, $B_1 = 0.25$, PLL parameters: $(60, 1400)$, converter current control parameters: $(0.3, 5)$.

If the effects of PLL dynamics and the feedforward filter are ignored and the PV is viewed as a current source only, the PCC voltage may reach 1.827 pu as shown in Fig. 17. The Bode plots of the admittance indicate that the qq component is resistive. Since the admittance is due to the effects of PLL and feedforward filter, it can be viewed as PLL and feedforward filter provide damping in the subcycle range. Hence, the overvoltage is less severe.

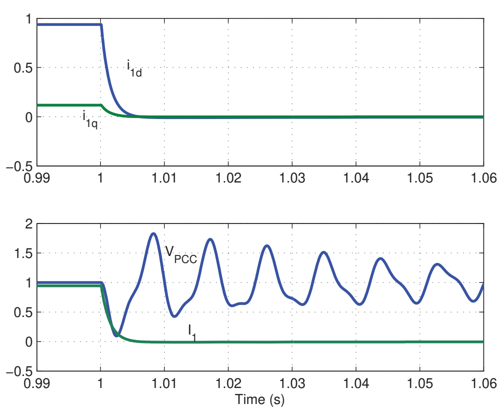

Fig. 17: Momentary cessation effect on the PCC voltage if the converter acts as a current source. $X_g = 0.5$, $B_1 = 0.25$.

D. Sensitivity Analysis

Impacts of grid strength (X_g), PLL parameters, and converter current control parameters are examined using eigenvalue loci generated by `tzero(Y)`.

Fig. 18a presents the system eigenvalue loci when the grid strength decreases. It can be seen that the mode at 60 Hz to 100 Hz moves to right while another mode at 200 Hz will move down and right. This trend indicates that subcycle overvoltage will be more severe should the grid strength reduces. This point has been verified by the simulation results of the EMT testbed and the simplified analytical model.

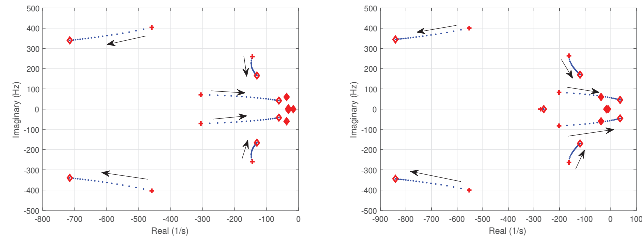

(a) (b)

Fig. 18: Comparison of different PLL parameters on eigenvalues. X_g varies from 0.26 to 0.60 pu, with each step 0.02 pu. B_1 is 0.25 pu. Converter current control parameters: $(0.3, 5)$. (a) PLL parameters: $(60, 1400)$.(b) PLL parameters: $(300, 3000)$.

Fig. 18b presents the eigenvalue loci when the grid strength reduces for a different PLL. The proportional and integral gains are 300 and 3000. This PLL has a higher bandwidth. It can be seen that the 60 Hz mode is influenced by PLL and this mode moves to the right half plane. The effect of PLL is also tested in time-domain simulation using the analytical model. See Fig. 19. It can be seen that for a PLL with higher bandwidth, the subcycle overvoltage is more severe and the converter voltage may reach 1.565 pu after 0.01 seconds. Note that for the same operation condition, for the PLL with a lower bandwidth, the converter voltage reaches 1.4 pu (See Fig. 10).

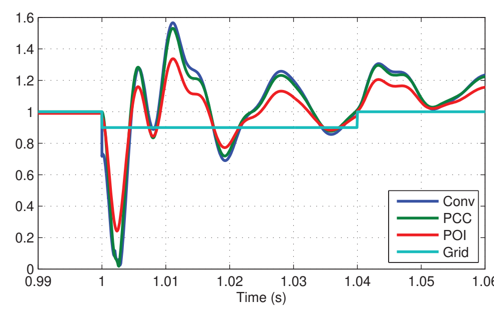

Fig. 19: Time-domain simulation results using the analytical model. X_g : 0.5 pu. PLL parameters: $(300, 3000)$. Converter current control parameters: $(0.3, 5)$. At $t = 1$, grid voltage has 10% dip and the current control orders change to 0.

Finally, the effects of current control parameters are compared. Fig. 20 presents the Bode plots of the admittance matrices for two types of current controllers. The solid lines correspond to the current control with proportional and integral gains at $(0.3, 5)$ while the dashed lines correspond to that with parameters at $(1, 15)$. The difference in the admittance frequency response is also manifested in time-domain simulation results in Fig. 21. For the current control with a larger gain, subcycle overvoltage appears slightly more severe.

E. Remarks and Discussion

In this paper, we have presented three types of models for subcycle dynamics investigation: (i) the EMT testbeds for validation and demonstration, (ii) nonlinear analytical model

This article has been accepted for publication in a future issue of this journal, but has not been fully edited. Content may change prior to final publication. Citation information: DOI 10.1109/TPWRD.2020.3016279, IEEE Transactions on Power Delivery

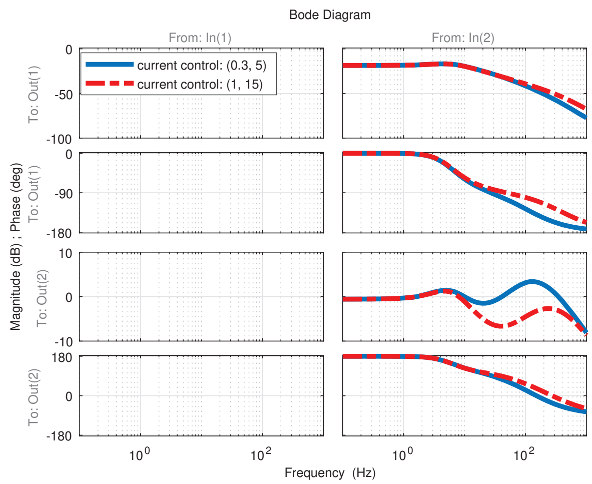

Fig. 20: Bode plots of the admittance for different current control parameters.

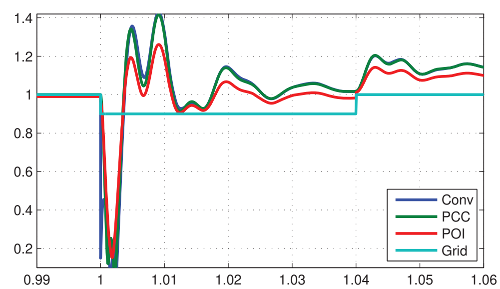

Fig. 21: Time-domain simulation results using the analytical model. X_g : 0.5 pu. PLL parameters: $(60, 1400)$. Converter current control parameters: $(1, 15)$. At $t = 1$, grid voltage has 10% dip and the current control orders change to 0.

for large-signal simulation, eigenvalue and participation factor analysis, and (iii) admittance model for circuit analysis. The EMT testbeds have full details modeled and are suitable for validation. However, EMT testbeds are not feasible for small-signal analysis. Thus, we seek models with the capability of small-signal analysis to provide insights of dynamics. The benefit of the nonlinear analytical model is its capability of both large-signal simulation and small-signal analysis. From the nonlinear analytical model, a linearized model can be obtained through numerical perturbation. Via the linear model, eigenvalue analysis and participation factor analysis clearly show that grid inductance, shunt capacitor are relevant to the modes associated to the subcycle dynamics. Finally, the admittance model is linear model based on derivation. The purpose of s-domain admittance-based circuit analysis is to further identify the mechanism of the dynamics and identify which factor is dominant. s-domain admittance model is suitable for small-signal analysis but not large-signal simulation..

From the circuit analysis, the mechanism of subcycle overvoltage dynamics can be identified as the LC dynamics due to PV farms' shunt compensation and grid's inductance reflecting grid strength. Under momentary cessation, the circuit is subjected to a step change in current injection from the converter. This sudden change excites subcycle overvoltage dynamics. Converter control effects have also been examined. Compared to grid strength, effects of converter control are much less significant in subcycle overvoltage phenomenon.

Occurrence of subcycle overvoltage dynamics is due to two prior conditions: PV farm has shunt compensation installed; the grid strength becomes weak due to transmission line tripping. On top of the existing conditions, PV systems' momentary cessation excites LC dynamics. Thus, quickly recovering grid strength from contingencies is of great importance for system operation with high penetration of PVs.

V. Conclusion

This paper reveals the mechanism of real-world dynamic phenomena observed recently in PV farms: subcycle transient overvoltage when PVs enter into momentary cessation mode. The dynamics are found to be associated with the LC dynamics related to shunt compensation and grid inductance. Converter controls, e.g., PLL dynamics, voltage feedforward, and current control parameters, more or less influence subcycle overvoltage dynamics. However, compared to PV shunt compensation and grid strength, they play a much less signifiant role.

References

[1] NERC. (2017, June) 1,200 MW Fault Induced Solar Photovoltaic Resource Interruption Disturbance Report: Southern California 8/16/2016 Event.

[2] Joint NERC and WECC Staff. (2018, February) 900 MW Fault Induced Solar Photovoltaic Resource Interruption Disturbance Report: Southern California Event: October 9, 2017.

[3] ——. (2019, January) April and May 2018 Fault Induced Solar Photovoltaic Resource Interruption Disturbances Report: Southern California Events: April 20, 2018 and May 11, 2018.

[4] P. Kundur, N. J. Balu, and M. G. Lauby, *Power system stability and control*. McGraw-hill New York, 1994, vol. 7.

[5] S. Skogestad and I. Postlethwaite, *Multivariable feedback control: analysis and design*. Wiley New York, 2007, vol. 2.

[6] E. I. Batzelis, G. Anagnostou, and B. C. Pal, "A state-space representation of irradiance-driven dynamics in two-stage photovoltaic systems," *IEEE Journal of Photovoltaics*, vol. 8, no. 4, pp. 1119–1124, 2018.

[7] E. Batzelis, G. Anagnostou, I. R. Cole, T. R. Betts, and B. C. Pal, "A state-space dynamic model for photovoltaic systems with full ancillary services support," *IEEE Transactions on Sustainable Energy*, 2018.

[8] L. Fan, "Modeling type-4 wind in weak grids," *IEEE Transactions on Sustainable Energy*, vol. 10, no. 2, pp. 853–864, April 2019.

[9] L. Fan and Z. Miao, "Wind in weak grids: 4 hz or 30 hz oscillations?" *IEEE Transactions on Power Systems*, vol. 33, no. 5, pp. 5803–5804, 2018.

[10] Y. Li, L. Fan, and Z. Miao, "Stability control for wind in weak grids," *IEEE Transactions on Sustainable Energy*, vol. 10, no. 4, pp. 2094–2103, 2018.

[11] ——, "Wind in weak grids: Low-frequency oscillations, subsynchronous oscillations, and torsional interactions," *IEEE Transactions on Power Systems*, vol. 35, no. 1, pp. 109–118, 2019.

[12] N. P. Strachan and D. Jovcic, "Stability of a variable-speed permanent magnet wind generator with weak ac grids," *IEEE Transactions on Power Delivery*, vol. 25, no. 4, pp. 2779–2788, 2010.

[13] J. Z. Zhou, H. Ding, S. Fan, Y. Zhang, and A. M. Gole, "Impact of short-circuit ratio and phase-locked-loop parameters on the small-signal behavior of a vsc-hvdc converter," *IEEE Transactions on Power Delivery*, vol. 29, no. 5, pp. 2287–2296, 2014.

[14] L. Harnefors, M. Bongiorno, and S. Lundberg, "Input-admittance calculation and shaping for controlled voltage-source converters," *IEEE transactions on industrial electronics*, vol. 54, no. 6, pp. 3323–3334, 2007.

[15] B. Wen, D. Boroyevich, R. Burgos, P. Mattavelli, and Z. Shen, "Analysis of dq small-signal impedance of grid-tied inverters," *IEEE Transactions on Power Electronics*, vol. 31, no. 1, pp. 675–687, 2015.

[16] B. Wen, D. Dong, D. Boroyevich, R. Burgos, P. Mattavelli, and Z. Shen, "Impedance-based analysis of grid-synchronization stability for three-phase paralleled converters," *IEEE Transactions on Power Electronics*, vol. 31, no. 1, pp. 26–38, 2016.

[17] "Pscad simple solar farm model." [Online]. Available: https://www.pscad.com/knowledge-base/article/521

[18] Z.-X. Zou and M. Liserre, "Modeling phase-locked loop-based synchronization in grid-interfaced converters," *IEEE Transactions on Energy Conversion*, 2019.

Lingling Fan (SM'08) received the B.S. and M.S. degrees in electrical engineering from Southeast University, Nanjing, China, in 1994 and 1997, respectively, and the Ph.D. degree in electrical engineering from West Virginia University, Morgantown, in 2001. Currently, she is a full professor at the University of South Florida, Tampa, where she has been since 2009. She was a Senior Engineer in the Transmission Asset Management Department, Midwest ISO, St. Paul, MN, form 2001 to 2007, and an Assistant Professor with North Dakota State University, Fargo, from 2007 to 2009. Her research interests include power systems and power electronics. Dr. Fan serves as the editor-in-chief for IEEE Electrification Magazine and associate editor for IEEE Trans. Energy Conversion.

Zhixin Miao (SM'09) received the B.S.E.E. degree from the Huazhong University of Science and Technology,Wuhan, China, in 1992, the M.S.E.E. degree from the Graduate School, Nanjing Automation Research Institute (Nanjing, China) in 1997, and the Ph.D. degree in electrical engineering from West Virginia University, Morgantown, in 2002.

Currently, he is with the University of South Florida (USF), Tampa. Prior to joining USF in 2009, he was with the Transmission Asset Management Department with Midwest ISO, St. Paul, MN, from 2002 to 2009. His research interests include power system stability, microgrid, and renewable energy.

Miao Zhang (S'15) received the B.S. degree in electrical engineering Hebei University of Architecture in 2012 and M.S. degree in electrical engineering from the University of South Florida (Tampa FL) in Dec 2017. He joined the University of South Florida Smart Grid Power Systems Lab in Jan, 2017 for Ph.D. study. His research interests include wind energy grid integration EMT modeling, power systems optimization, system identification, and data analysis.